

Vacancy-Driven Gelation Using Defect-Rich Nanoassemblies of 2D Transition Metal Dichalcogenides and Polymeric Binder for Biomedical Applications

Manish K. Jaiswal,* James K. Carrow, James L. Gentry, Jagriti Gupta, Nara Altangerel, Marlan Scully, and Akhilesh K. Gaharwar*

A new approach of vacancy-driven gelation to obtain chemically crosslinked hydrogels from defect-rich 2D molybdenum disulfide (MoS_2) nanoassemblies and polymeric binder is reported. This approach utilizes the planar and edge atomic defects available on the surface of the 2D MoS_2 nanoassemblies to form mechanically resilient and elastomeric nanocomposite hydrogels. The atomic defects present on the lattice plane of 2D MoS_2 nanoassemblies are due to atomic vacancies and can act as an active center for vacancy-driven gelation with a thiol-activated terminal such as four-arm poly(ethylene glycol)-thiol (PEG-SH) via chemisorption. By modulating the number of vacancies on the 2D MoS_2 nanoassemblies, the physical and chemical properties of the hydrogel network can be controlled. This vacancy-driven gelation process does not require external stimuli such as UV exposure, chemical initiator, or thermal agitation for crosslinking and thus provides a nontoxic and facile approach to encapsulate cells and proteins. 2D MoS_2 nanoassemblies are cytocompatible, and encapsulated cells in the nanocomposite hydrogels show high viability. Overall, the nanoengineered hydrogel obtained from vacancy-driven gelation is mechanically resilient and can be used for a range of biomedical applications including tissue engineering, regenerative medicine, and cell and therapeutic delivery.

2D transition metal dichalcogenides (TMD), such as molybdenum disulfide (MoS_2), have gained unprecedented attention due to their unique atomically thin, layered, and well-defined structure that provides distinctive physical and chemical properties compared to bulk 3D counterparts.^[1,2] 2D TMDs have high electron density and facile formation of lattice atomic defects, enabling researchers to explore a wide variety of applications in nanoelectronics,^[3,4] energy,^[5,6] optics, sensors,^[2] catalysis,^[7] photothermal agents for cancer treatments,^[8,9] and biomedical research.^[10] Despite interesting properties of 2D TMDs, they are not extensively investigated for regenerative medicine due to an inability to incorporate within biomaterial scaffolds.

Here, we demonstrate a new approach of chemically conjugating 2D MoS_2 with polymeric binder to form high-water content gels. This new approach of chemical conjugation between 2D nanomaterials

and polymeric chains utilizes the planar and edge atomic defects^[11] available on these nanomaterials. This will generate a chemically reinforced polymeric network thereby promoting the formation of mechanically resilient networks. The role of the atomic defects present on the lattice plane of 2D MoS_2 to serve as an efficient catalyst in electrochemical production of hydrogen has been well studied.^[7,12] These atomic defects are mostly due to sulfur vacancies and can act as an active center for catalysis. Molybdenum (Mo) is thiophilic^[3] and sulfur (S) has a strong affinity toward forming disulfide bond,^[13] together they offer facile binding centers for thiolated molecules. Some recent works have demonstrated this ability of the 2D MoS_2 nanosheets via thiol-activated ligand conjugation.^[14] We intend to exploit these vacancy-driven active centers to conjugate macromolecules with thiol-activated terminal such as poly(ethylene glycol)-thiol (PEG-SH) via chemisorption to form elastomeric and robust gel.

In 2D MoS_2 , molybdenum occupies a trigonal prismatic (Mo^{IV}) coordination and bound to six sulfide ligands. Sulfur occupies a pyramidal (S^{2-}) location and is coordinated with three molybdenum atoms. This results in the formation of a layered structure with interconnected trigonal prisms, wherein

Dr. M. K. Jaiswal, J. K. Carrow, J. L. Gentry, Prof. A. K. Gaharwar
Department of Biomedical Engineering
Texas A&M University
College Station, TX 77843, USA
E-mail: manish@tamu.edu; gaharwar@tamu.edu

Dr. J. Gupta
Department of Metallurgical Engineering and Materials Sciences
Indian Institute of Technology Bombay
Mumbai 400076, India

N. Altangerel, Prof. M. Scully
Department of Physics
Texas A&M University
College Station, TX 77843, USA

Prof. A. K. Gaharwar
Department of Materials Science and Engineering
Texas A&M University
College Station, TX 77843, USA

Prof. A. K. Gaharwar
Center for Remote Health Technologies and Systems
Texas A&M University
College Station, TX 77843, USA



The ORCID identification number(s) for the author(s) of this article can be found under <https://doi.org/10.1002/adma.201702037>.

DOI: 10.1002/adma.201702037

molybdenum atoms are sandwiched between layers of sulfur atoms. Therefore, pristine MoS₂ structures provide minimum planar defects and lack sufficient active centers for conjugation with polymeric molecules. To overcome this issue, we synthesized defect-rich MoS₂ nanosheets by constraining the growth of the lattice to include atomic defects. By modulating the precursor mole ratios of molybdenum:sulfur (1:1 to 1:2, 1:4, and 1:6), a series of nanosheets with various degrees of defects were obtained (Figure 1a). We have used hexaammonium heptamolybdate and thiourea as precursor for molybdenum and sulphur, respectively (see Supporting Information). The MoS₂ nanosheets assemble to form cocentric, well-segregated, hierarchical structures which resemble a flower (MoS₂ nanoassembly) wherein the nanosheet flakes form petals.^[6,15,16] The formation of MoS₂ nanoassemblies occurs mainly due to Ostwald ripening of flakes grown during hydrothermal process at higher temperature.^[8] Due to the rippled morphology, MoS₂ nanosheets remain unstacked and provide larger surface area and easy access to planar defects.

The aqueous stability of MoS₂ nanoassemblies was investigated by zeta potential (ζ) measurements. Nanoassemblies were stable in water with ζ in the range of -35 mV ($\pm 10\%$). No significant difference in zeta potential was observed due to change in Mo:S ratios; however, increase in thiourea content resulted in enhanced aqueous stability. The hierarchical nanoassemblies were analyzed by scanning electron microscopy (SEM) and showed a typical size of ≈ 1.5 – 2 μm (Figure 1b). The effect of thiourea precursor ratio (1:1, 1:2, 1:4, 1:6) and aging time (6, 18, and 30 h) on the morphological features of nanoassemblies were also investigated. Following an increase in thiourea precursor ratio, the MoS₂ flakes tended to grow and evolved rapidly, resulting in fully exfoliated and expanded flower-like morphology (Figure S1a, Supporting Information). The aging time also had significant effect on the structure of nanoassemblies. We observed that 18 h is required to obtain fully exfoliated, rippled nanoassemblies (Figure S1b, Supporting Information), while no significant effect was observed for longer aging time (30 h).

We then confirmed the hexagonal arrangement (2H phase) of 2D MoS₂, where each Mo atom is coordinated with three in-plane sulfur atoms at 120° , using X-ray diffraction (XRD), selected area electron diffraction (SAED), and X-ray photoelectron spectra (XPS). The diffraction peaks of nanoassemblies (002, 004, 100, 103, 006, 105 and 110) agree well with the hexagonal MoS₂ (JCPDS card No. 73-1508), indicating the high purity of synthesized MoS₂ (Figure 1c). The gradual decrease in peak broadness (002) as characterized by full width at half maximum (FWHM) using the Scherrer equation indicated an increase in crystallite size. FWHM for 1:1 (Mo:S) was 1.137 radians, which reduced to 0.893 radians for 1:6 (Mo:S). The crystallite size, calculated from Scherrer equation, increased from 7.82 nm for 1:1 ratio to ≈ 9.96 nm for 1:6 ratio sample. These findings suggest the formation of more ordered phase of MoS₂ with increasing thiourea content, which correlates with previous reports.^[16,17] The representative transmission electron microscopy (TEM) images along with the SAED pattern indicated the crystalline nature of 2D MoS₂ nanoassemblies (Figure 1d). The indexed SAED patterns corroborated the MoS₂ lattice planes observed in XRD pattern. The rippled morphology of MoS₂

nanoflakes provides easy access to active centers as it inhibits flake stacking. The XPS of MoS₂ nanoassemblies were deconvoluted for Mo and S (Figure 1e). XPS data indicate the binding energies of Mo⁴⁺ 3d_{5/2} (228.31 eV) and 3d_{3/2} (231.46 eV), while for S²⁻ 2p_{3/2} (161.06 eV) and 2p_{1/2} (162.25 eV). The difference in binding energy between Mo⁴⁺ 3d_{5/2} and 3d_{3/2} was $\Delta = 3.15$ eV, which further confirmed the formation of dominant 2H phase. These observations indicate the formation of defect-rich MoS₂.

The number of active centers (or defect sites) available on 2D MoS₂ nanoassemblies was determined by Raman spectroscopy and cyclic voltammetry. From the Raman spectra (Figure 1f), in-plane vibrations of two S atoms with respect to Mo (E_{2g}^1) were blue-shifted from sample 1:1 (374.3 cm⁻¹) to 1:6 (376.5 cm⁻¹), while the out-of-plane vibration of single S atom, A_{1g} (401.8 cm⁻¹) remained the same for all samples. Raman spectroscopy is a strong tool to ascertain increased built-in lattice strain by changes occurring at the E_{2g}^1 peak position, which can be attributed to the rippled morphology of the crystal. Furthermore, the peak intensity of A_{1g} , which otherwise signifies the interlayer van der Waals interactions, was amplified with an increase in thiourea content, more so, the ratio of A_{1g}/E_{2g}^1 was significantly enhanced from 1:1 (0.7) to 1:6 (2.3) nanoassemblies. This further demonstrates the presence of unsaturated lattice atoms and increased crystal layer thickness, as predicted by Scherrer formula in XRD data which eventually give rise to high-intensity Raman peaks.^[18] We further used cyclic voltammetry to determine the number of active centers. The density of the active centers in 1:1 was found to be 0.59×10^{-4} moles g⁻¹, which increased to 2.10×10^{-4} moles g⁻¹ for 1:6 (Figure S2, Supporting Information). To further validate the presence of defect sites, we performed photoluminescence (PL) spectra of nanoassemblies, as an increase in defect sites directly affects photoluminescence characteristics of 2D MoS₂. A strong UV absorption peak was observed at 470 nm for MoS₂ nanoassemblies (Figure S3, Supporting Information). Therefore, we carried out the PL spectra of these nanoassemblies by exciting at 470 nm and recording the emission spectra between 550 and 700 nm (Figure 1f). The gradual amplification in peak intensities (580, 610, and 680 nm) from 1:1 to 1:6 samples can be attributed to the increased number of defects in the crystal lattice. For lower precursor ratios (e.g., 1:1 and 1:2), due to oriented growth of the crystals, we observed fewer atomic vacancies; however, the excess addition of thiourea resulted in confined MoS₂ growth and generated more atomic vacancies. Overall, these results suggested that with the increase in thiourea concentration, the number of active centers (or defect site) was also increased.

We hypothesize the defect-rich MoS₂ nanoassemblies provide abundant active centers for covalent binding with multiarm poly(ethylene glycol)-thiol (four-arm PEG-SH). Molybdenum from MoS₂ nanoassemblies maintains preferential conjugation to sulfur from PEG-SH and results in the formation of covalently crosslinked network (Figure 2a). The potential of defect-rich MoS₂ nanoassemblies for the gelation of a polymeric network has not been previously reported to our knowledge. By controlling the concentration of MoS₂ nanoassemblies, gelation kinetics, mechanical stiffness, and physiochemical characteristics of the hydrogel network can be modulated. The advantages

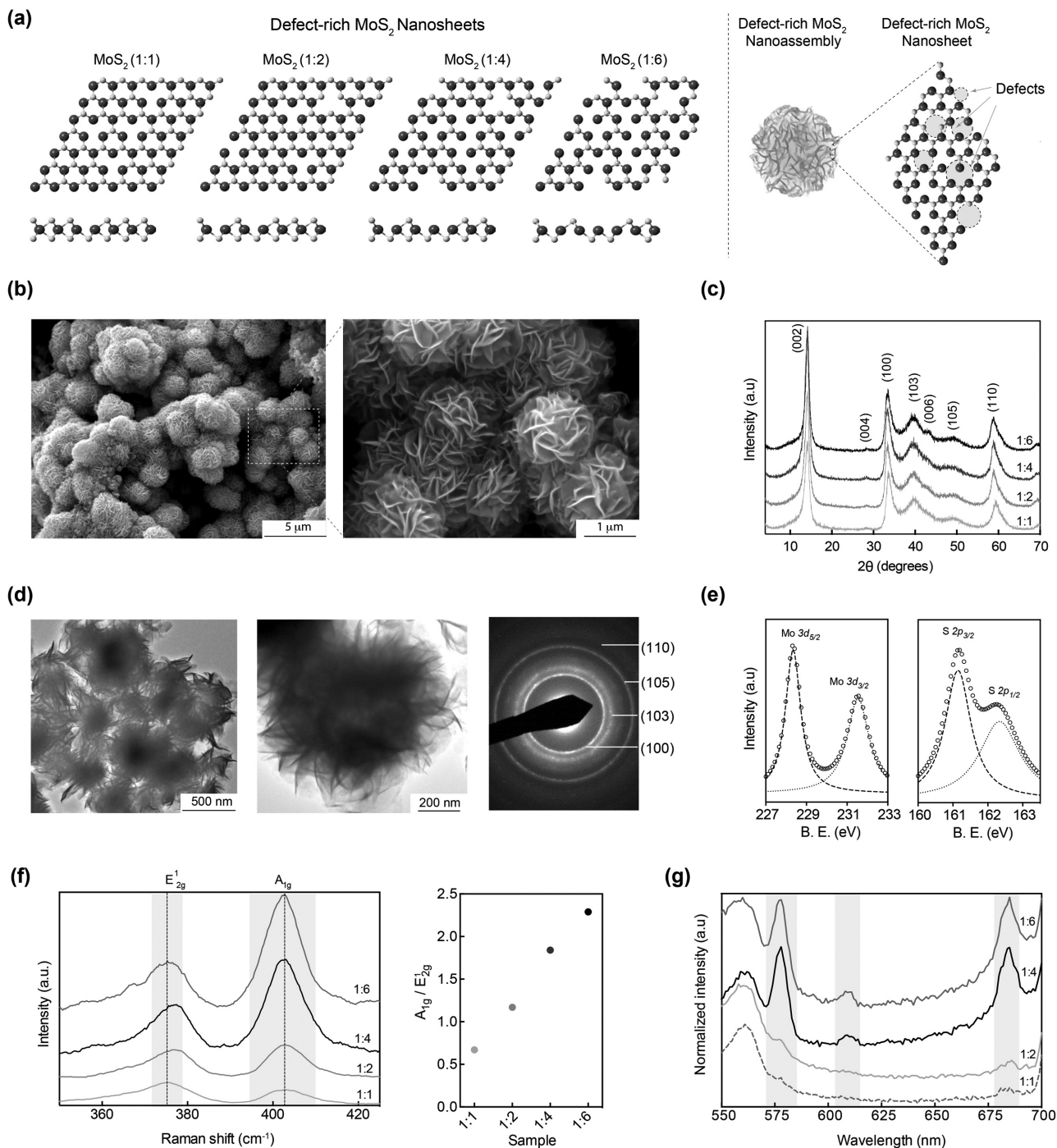


Figure 1. Defect-rich MoS₂ nanoassemblies. a) The atomic lattice of MoS₂ with different Mo:S ratio, where each molybdenum atom is coordinated by six sulfur atoms at 120° each, giving it hexagonal arrangement. Atomic vacancies can be created by confined growth of the lattice. Defect-rich 2D MoS₂ assemblies form spherical nanoassemblies. b) SEM image of nanoassemblies shows rippled flakes arranged spherically. c) The 2H phase of MoS₂ lattice was confirmed by X-ray diffraction pattern obtained for different feed precursor ratios (molybdenum:sulfur). d) TEM of the nanoassemblies along with selected area electron diffraction (SAED) confirmed hierarchy of assembled nanostructure. e) X-ray photoelectron spectroscopy of MoS₂ samples analyzed for Mo and S binding energies confirm the hexagonal arrangement. f) Raman spectra confirmed the presence of two prominent peaks (E_{2g}¹ and A_{1g}) corresponding to 2H phase, while their intensity ratio supported the consistent increment in intensity related to out-of-plane vibration of S atoms with increase in sulfur feed precursor ratio. g) Photoluminescence (PL) spectra of MoS₂ nanoassemblies depicting the evolution of signals due to defect sites and were directly proportional to the number of active centers.

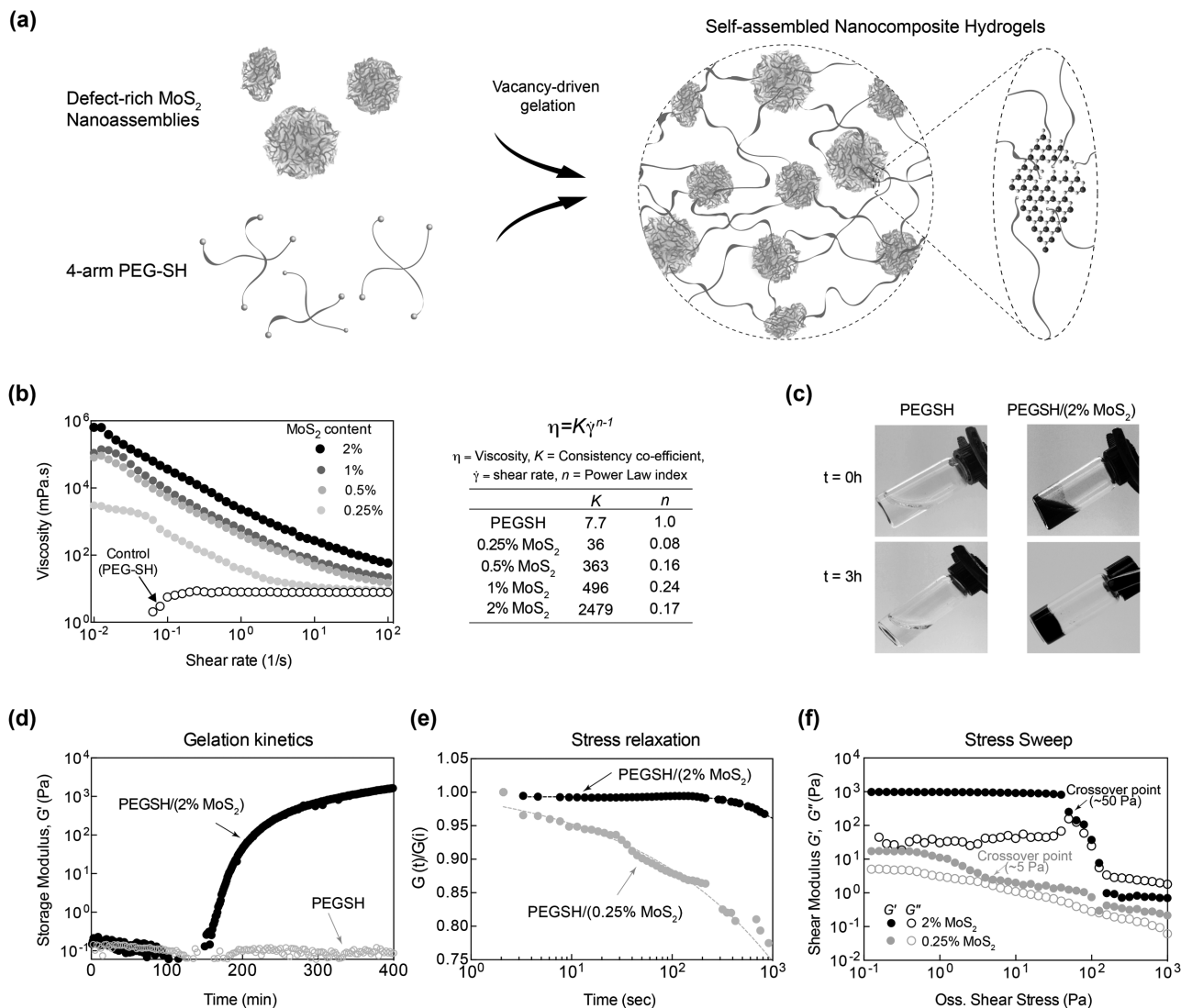


Figure 2. Vacancy-driven gelation of MoS₂ and PEG-SH. a) The presence of vacancies in MoS₂ provides active centers for chemisorption (Mo-S and S-S interactions) of thiolated polymer chains (four-arm PEG-SH) leading to formation of crosslinked hydrogels. b) Shear-thinning characteristic of prepolymer solutions. 10% PEG-SH show Newtonian behavior. The viscosity of prepolymer solutions increases with the addition of MoS₂ and display shear-thinning characteristics. Power law model was fitted to determine power law index and consistency coefficient. c) Photographs showing formation of crosslinked hydrogels from PEG-SH/2%MoS₂. While PEG-SH remain sol after 3 h. d) Gelation kinetics of PEG-SH and PEG-SH/2%MoS₂ confirm vacancy-driven gelation of defect-rich MoS₂ nanoassemblies and PEG-SH. e) Stress relaxation behavior of crosslinked hydrogels revealing higher network stability with 2% MoS₂ compared to 0.25% MoS₂ under 5% strain. f) Stress sweep indicating stability of crosslinked gel under shear stress.

of this vacancy-driven gelation process are it does not require external stimuli such as UV exposure and thermal agitation and provide facile approach to encapsulate cells and proteins for biomedical applications.

Due to presence of active centers, it is expected that MoS₂ nanoassemblies will strongly interact with PEG-SH. To investigate these interactions, the viscosity of prepolymer solution was determined at different shear rates using a rheometer (Figure 2b). The shear-thinning characteristics of prepolymer solution was investigated by fitting power law (or Ostwald) model. The power law index (n), calculated from fitting viscosity ($\eta = K\dot{\gamma}^{n-1}$), where K is consistency factor and $\dot{\gamma}$ is shear rate. A Newtonian fluid will have $n = 1$, while a shear-thinning fluid will have $0 < n < 1$. The viscosity of PEG-SH is unchanged at

shear rate from 0.01 to 100 s⁻¹, indicating Newtonian behavior. However, with the addition of MoS₂ nanoassemblies (1:4), viscosity of the prepolymer solution changes significantly and displays a shear-thinning characteristic ($n < 0.3$). For example, the viscosity of PEG-SH/2%MoS₂ was 10⁶ mPa s at low shear (0.01 s⁻¹) which drastically reduced to about 10 mPa s at 100 s⁻¹.

The addition of MoS₂ nanoassemblies to PEG-SH induced vacancy-driven gelation. The gelation phenomenon is evident from the photographic images of the PEG-SH and PEG-SH/MoS₂ compositions (Figure 2c). The gelation kinetics was monitored by placing the prepolymer solution containing four-arm PEG-SH (10%, $M_w \approx 20\,000$) and MoS₂ nanoassemblies (2%) in deionized (DI) H₂O, and monitoring storage modulus (G')

overtime (Figure 2d). The PEG–SH solution does not form gel as G' remained unchanged over 6 h, while the addition of 2% MoS₂ resulted into crosslinked hydrogel within 4 h as G' plateau at 3 kPa. This indicated that the chemisorption of sulfur atoms via Mo–S interactions between MoS₂ nanoassemblies and PEG–SH transformed the polymer network into a viscoelastic gel.

By modulating the number of defect sites, gelation kinetics can be controlled. The gelation kinetics of prepolymer solutions containing PEG–SH and different ratios of MoS₂ nanoassemblies (1:1, 1:2, and 1:6) were investigated (Figure S4, Supporting Information). The results show that the number of defects in MoS₂ nanoassemblies controls the gelation kinetics and mechanical strength of crosslinked network. For example, with an increase in vacancy sites rapid gelation and stiffer network were formed. Other parameters that can be modulated to obtain desired gelation kinetics and mechanical properties are molecular weight and/or number of thiol-activated terminals in polymeric binder. For example, shorter chain length of polymeric binder might result in significantly higher crosslinking density and limited elastomeric characteristics, while long-chain polymeric binder might promote elastomeric characteristics of nanocomposite hydrogels. It is possible that if chain lengths of polymeric binders are shorter, thiol-activated terminals present on polymeric binder might conjugate on same MoS₂ nanoassemblies and may result in lower mechanical stiffness.

The network stability of the crosslinked gels is highly dependent on the molybdenum–sulfur interactions, further highlighted by stress-relaxation experiments (Figure 2e, and Figure S5, Supporting Information). The crosslinked hydrogel (2 mm thick) was subjected to 5% strain (γ) at 1 Hz and stress, σ , was determined as a function of time (t). Normalized relaxation modulus was calculated as $G(t)/G(i)$, where nonlinear shear relaxation modulus is defined as $G(t) = \sigma(t)/\gamma$ and instantaneous modulus as $G(i)$. The results showed a significant change in stability of the network with higher MoS₂ concentration over a longer time. The hydrogel with low MoS₂ concentration (PEG–SH/0.25%MoS₂) relaxed rapidly (≈ 40 s) and dissipated more than 25% of initial strain energy within 1000 s. While hydrogel loaded with higher concentration of MoS₂ (PEG–SH/2%MoS₂) did not dissipate its strain energy and maintained network stability, indicating a greater prevalence of Mo–S interactions between PEG–SH and MoS₂ nanoassemblies. Furthermore, the network stability was also determined using oscillatory shear sweep experiments (Figure 2f). The crossover of G' and G'' , which essentially signifies the dynamics of network rupture, occurred at ≈ 5 Pa for PEG–SH/0.25%MoS₂ hydrogels and ≈ 50 Pa for PEG–SH/2%MoS₂. From the stress sweep experiment, we also determined yield strain of the crosslinked networks, where G' deviate from the linear viscoelastic region (LVR). An increase in yield strain from 1 to 5% was observed with an increase in MoS₂ concentration from 0.25 to 2%, respectively. The increase in crossover point and yield strain due to increase in MoS₂ concentration indicates that the hydrogel loaded with 2%MoS₂ is mechanically stable compared to hydrogel loaded with 0.25%MoS₂.

The crosslinked hydrogels (PEG–SH/2%MoS₂) showed remarkable mechanical resilience and could be stretched,

bended, and twisted easily (Figure 3a). These hydrogels could be twisted five times without fracture (Figure S6, Supporting Information), indicating its potential use in several biomedical applications under dynamic mechanical environments. The hydrogels were further characterized via uniaxial compression test to determine compressive modulus from stress–strain curves. Due to a lack of gelation, PEG–SH compositions lacking MoS₂ were not evaluated. The addition of MoS₂ to PEG–SH resulted in linear increase in compressive modulus from 8.6 ± 0.6 kPa (PEG–SH/0.25%MoS₂) to 27.7 ± 1.1 kPa (PEG–SH/2%MoS₂) (Figure 3b). Elastomeric characteristics of crosslinked hydrogels were investigated using cyclic compression (40% compressive strain). All PEG–SH/MoS₂ hydrogels displayed >99% recovery in compressive modulus following four cycles (Figure S7, Supporting Information). These results demonstrated the mechanical robustness and elasticity of PEG–SH/MoS₂ hydrogels, highlighting the role of active centers present on MoS₂ sheets to chemically conjugate with PEG–SH.

We further carried out scanning electron microscopy (SEM) of the transverse section of freeze-dried hydrogels to determine the distribution of MoS₂ nanoassemblies within the crosslinked network (Figure 3c). SEM images show interconnected porous network with pore size ≈ 10 μ m. We further confirmed the presence of MoS₂ nanoassemblies using energy-dispersive X-ray spectra (EDS). The EDS mapping of the selected area for Mo and S clearly confirms the presence of MoS₂ nanoassemblies interconnected with polymer.

To investigate the gelation mechanism, Raman and X-ray photoelectron spectroscopy (XPS) were performed to determine the chemical conjugation between MoS₂ nanoassemblies and PEG–SH. It was expected that the vacancy-driven gelation involved Mo (from MoS₂ nanoassemblies) and S (from PEG–SH) as well as possible disulfide linkages between PEG–SH and S (from MoS₂ nanoassemblies). Four-arm PEG–SH interactions with Mo on the MoS₂ lattice formed Mo–S bond due to chemisorption at the active centers (or defect sites). Raman spectra analysis of PEG–SH shows two thiol peaks at about 670 cm^{−1} (due to –SH deformation) and 2570 cm^{−1} (due to –SH stretching) (Figure 4a). These peak intensities reduced significantly when the hydrogel was formed in presence of 0.25% MoS₂ and completely disappeared when 2% MoS₂ was added. An overall attenuation in the characteristic Raman signatures of PEG–SH in the nanocomposites was observed. This might be due to the presence of MoS₂ nanoassemblies and/or porous nature of the dried hydrogel network which hinders the number of molecules from the polymer chain to interact with the incident laser beam and produce Raman signals. In nanocomposite samples, the disappearance of thiol peaks demonstrates the chemisorption of sulfur (from PEG–SH) to the MoS₂ lattice due to the strong affinity of Mo atoms toward sulfur. In addition, two additional peaks at 377 and 402 cm^{−1} belonging to E_{1g} (in-plane vibration of S atoms with respect to Mo) and A_{1g} (out-of-plane vibration of S atom) of MoS₂ were also affected due to crosslinking. For example, A_{1g}/E_{1g} ratio for MoS₂ nanoassemblies (1:4) was 1.9, while for crosslinked hydrogels A_{1g}/E_{1g} ratio was 2.05 (PEG–SH/0.25%MoS₂) and 3.44 (PEG–SH/2%MoS₂), indicating an increase in van der Waals interactions from crosslinking between MoS₂ nanoassemblies and polymer chains.

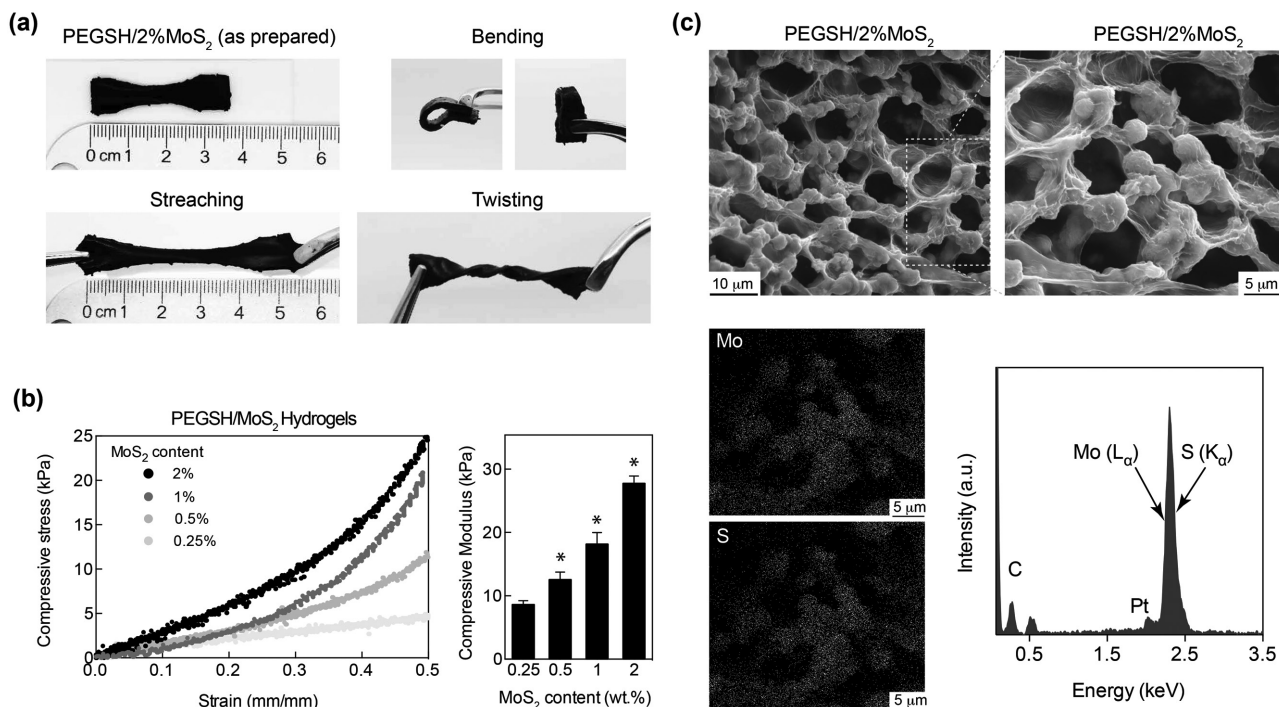


Figure 3. Mechanically stiff and elastomeric hydrogel from defect-rich MoS₂ nanoassemblies and PEG-SH. a) Photographs of crosslinked hydrogels (PEG-SH/2% MoS₂) show high mechanical flexibility. Crosslinked hydrogels can sustain stretching, bending, and twisting without plastic deformation and can recover back to original shape. b) Uniaxial compression demonstrates formation of mechanically stiff hydrogel network. The compressive modulus increases from 8 to 25 kPa with an increase in MoS₂ concentration from 0.25 to 2%. c) SEM images of a transverse section of hydrogel (PEG-SH/2% MoS₂) show porous and interconnect network. Energy-dispersive X-ray spectroscopy (EDS) spectra and mapping confirmed the presence of Mo and S in the crosslinked network.

To corroborate the Raman data on gelation mechanism, we carried out XPS analysis of carbon 1s and molybdenum 3d core level electrons from covalently crosslinked hydrogels and compared them with PEG-SH and MoS₂ (Figure 4b). From carbon (1s) spectra, peaks belonging to sp², C-C, C-O, and C-S in PEG appeared at 284.1, 284.7, 285.1, and 286.5 eV, respectively. Binding energies for all peaks decreased after gelation, while the C-S peak decreased significantly due to direct interaction of molybdenum from MoS₂ with PEG-SH, which facilitates C-S-Mo formation. From molybdenum (3d) spectra, the peaks of 3d_{5/2} and 3d_{3/2} from MoS₂ shifted following gelation. In addition, Mo spectra from crosslinked hydrogels revealed formation of two new bands when compared with pristine MoS₂. Specifically, new peaks appeared at 228.2 and 235.2 eV, which can be attributed to the formation of C-S-Mo due to chemisorption of sulfur. Overall, both Raman and XPS confirmed vacancy-driven gelation mechanism between MoS₂ nanoassemblies and PEG-SH.

To evaluate the biomedical application of 2D MoS₂ nanoassemblies, we first investigated the interaction between nanoassemblies and mouse preosteoblast cells (MC3T3 E1-sub-clone 4). As limited studies have investigated MoS₂ nanoassemblies for biomedical applications, we evaluated morphology of cells in presence of MoS₂ nanoassemblies. Bright-field microscopy revealed that MoS₂ nanoassemblies (10 μg mL⁻¹) readily attach to cell membrane and potentially internalized by cells via endocytosis (Figure 5a). The cells showed normal spindle shape phenotype in presence of MoS₂ nanoassemblies, and no

adverse toxicity was observed at macroscopic level. Following these initial assessments, cytotoxicity assay was performed after cells were subjected to increasing concentration of MoS₂ nanoassemblies (0–10 mg mL⁻¹) (Figure 5b). The cell viability was not affected at lower concentration of MoS₂ nanoassemblies (<100 μg mL⁻¹). At higher MoS₂ nanoassemblies concentration (100 μg mL⁻¹ to 10 mg mL⁻¹), a decrease in cellular viability was observed ≈60%. It is possible that at higher concentrations, MoS₂ nanoassemblies limit cellular function through activation of intracellular stress responses. Despite subjecting cells to 10 mg mL⁻¹ MoS₂ nanoassemblies, half maximal inhibitory concentration (IC₅₀) was not observed, while other 2D nanomaterials such as nanosilicates and graphene have IC₅₀ of ≈5 and ≈1 mg mL⁻¹, respectively.^[19] To investigate the effect of MoS₂ nanoassemblies on cell proliferation, cell cycle analysis was performed (Figure 5c). At lower MoS₂ concentration (≈10 μg mL⁻¹), no significant change in the G2/M population was observed, however at higher concentrations (≈100 and 1000 μg mL⁻¹), a significant decrease in G2/M cell population was observed signifying a shift into a lower proliferative state. Moreover, at higher concentrations, a significant increase in the apoptotic population was also observed, supporting the cell viability assay. Overall, these studies demonstrate the cytocompatibility of these nanomaterials, particularly in comparison to other types of 2D nanomaterials. Furthermore, these results indicate the eventual degradation products of PEG-SH/MoS₂ gels would not inhibit normal cellular function in the surrounding tissue.

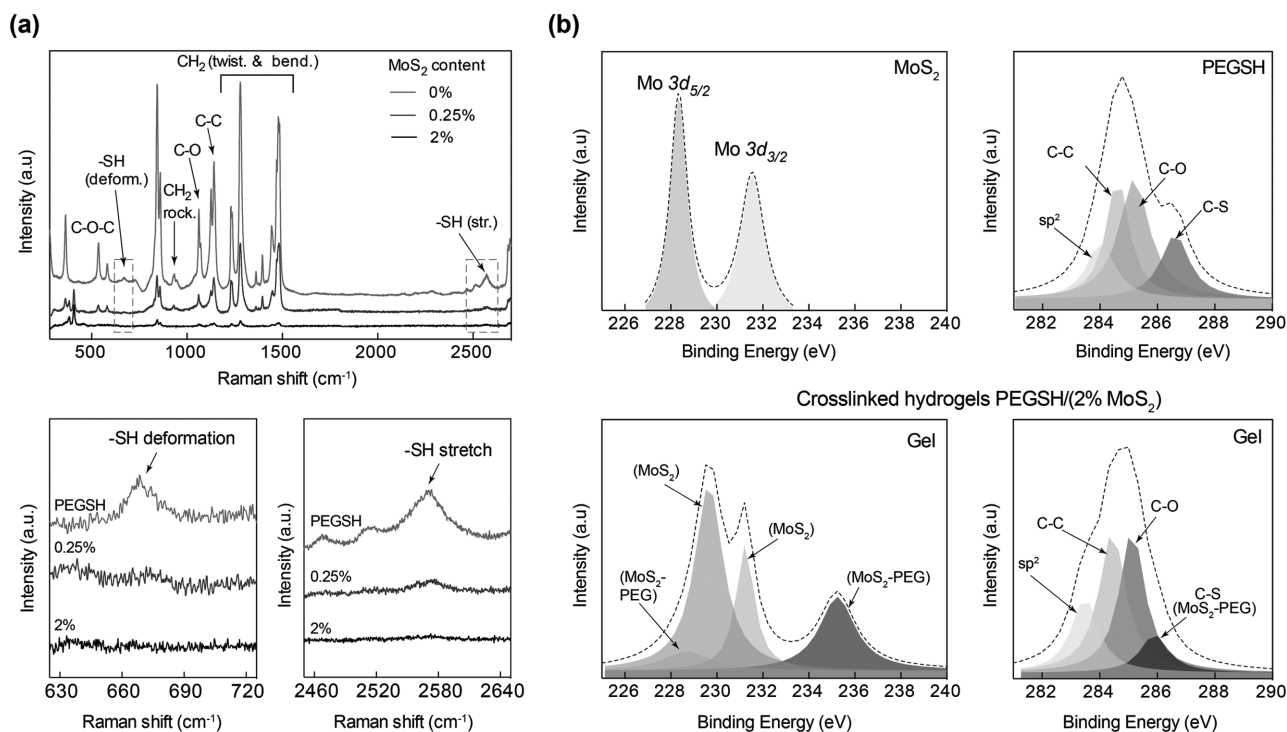


Figure 4. Chemical confirmation of vacancy-driven gelation. a) Raman spectra of PEG-SH along with gels made with 0.25 and 2% MoS₂. The thiol vibrations at 670 and 2570⁻¹ from PEG disappeared in the crosslinked hydrogels due to formation of new bond with MoS₂. b) XPS of hydrogel shows the change in binding energy of carbon (C 1s) peak due to C-S-Mo formation while two additional peaks appeared in Mo 3d spectrum belonging to PEG-MoS₂. Raman and XPS together suggest the new bond formation at the site of vacancy via chemisorption.

The facile synthesis of nanocomposite hydrogels via vacancy-driven gelation between MoS₂ nanoassemblies and PEG-SH can be used to encapsulate and deliver cells for regenerative medicine. To confirm the ability of hydrogel formation in cell culture media (α -MEM), we mixed MoS₂ nanoassemblies and PEG-SH and monitored the gelation kinetics using rheometer. A significant reduction in gelation time and increase in storage modulus ($G' \approx 11$ kPa) in 1.5 h was observed (Figure 5d). The improved gelation kinetics in cell culture media compared to DI water might be attributed to the presence of mineral ions that facilitate the vacancy-driven reaction. The stability of nanocomposite hydrogels in cell culture media was monitored for 48 h to evaluate its ability to support encapsulated cells (Figure 5e). PEG-SH/2%MoS₂ hydrogels readily swelled (4–6 times) in media and retained the initial shape. However, a significant dissociation was observed in solutions containing excess thiols (e.g., dithiothreitol (DTT)), indicating a breakdown of thiol-based linkages between PEG-SH and MoS₂ nanoassemblies. The stability of nanocomposites hydrogels in media is expected to limit the immediate release of MoS₂ nanoassemblies, maintaining concentrations within cytocompatible ranges.

Due to facile crosslinking process, we can encapsulate cells within the nanocomposite hydrogel network. As no photoinitiator or radical initiators were used, it is expected that cells will be able to survive the gelation process. We added cells to prepolymer solutions containing 10% PEG-SH and 2% MoS₂ nanoassemblies in cell culture media. The gelation was allowed by placing the gel solution within a well plate and incubated at 37 °C. Cells survive the gelation process and maintain high

viability after 48 h, as evident by high number of live (green) cells compared to dead cells (red) (Figure 5f). This shows that vacancy-driven gelation between MoS₂ nanoassemblies and PEG-SH has the potential to deliver cells for regenerative medicine.

Overall, we demonstrated a new approach to form chemically crosslinked hydrogels by utilizing vacancies in 2D TMDs and polymeric binder. This approach explored planar and edge atomic defects available on 2D nanomaterials, which can be easily generalized to other 2D nanomaterials. We successfully synthesized a range of defect-rich MoS₂ nanoassemblies by allowing the confined growth of the lattice with atomic defects. These defect-rich MoS₂ nanoassemblies provided abundant active centers for covalently binding multiarm PEG thiol. The addition of MoS₂ nanoassemblies to PEG-SH induced vacancy-driven gelation and results in covalently crosslinked hydrogel networks. Molybdenum, from MoS₂ nanoassemblies, demonstrated preferential conjugation to sulfur from PEG-SH. As nanoassemblies can have controlled generation of active sites, conjugation to multiple polymeric chains is enabled, virtually acting as a crosslink epicenter to reinforce polymeric hydrogels. Mechanically robust and elastic hydrogels were formed using this facile process without external stimuli such as UV exposure, thermal agitation, chemical radical, etc. MoS₂ nanoassemblies and nanocomposite hydrogels are cytocompatible and can be used to encapsulate cells. The vacancy-driven gelation approach can be used for a range of biomedical applications including tissue engineering, regenerative medicine, and cell and therapeutic delivery. In addition, the hydrogels loaded with

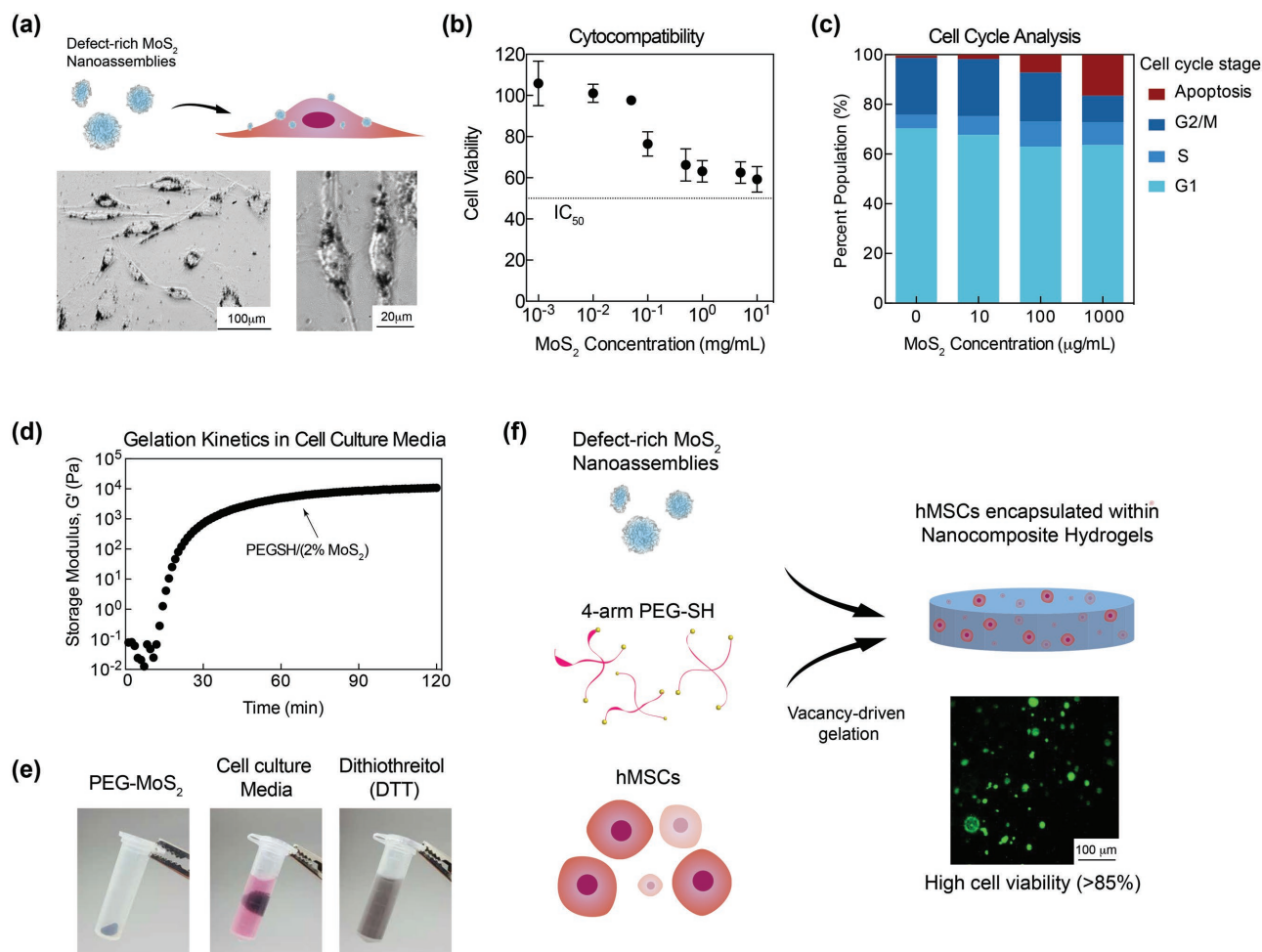


Figure 5. In vitro cytocompatibility of MoS₂ nanoassemblies and PEG-SH/MoS₂ hydrogels. a) MoS₂ nanoassemblies readily adhere to cell membrane (dark area) and do not alter cellular morphology. b) The viability of cells in presence of different concentrations of MoS₂ nanoassemblies was determined using MTT cytotoxicity assay. c) The effect of MoS₂ nanoassemblies on cell cycle was evaluated using flow cytometry. The results show that high cell population in G2/M phase at lower MoS₂ concentration shifts to apoptosis phase at higher MoS₂ concentrations. d) Gelation kinetics of PEG-SH and 2% MoS₂ nanoassemblies (1:4) in culture media exhibited accelerated gelation and stiffer network due to the presence of mineral ions in the media. e) The physical stability of gel in culture media as well as in excess thiol was determined. While the gel maintains its structural integrity in culture media, it gets dissolved in DTT due to presence of excess thiol. f) The facile vacancy-driven gelation between PEG-SH and MoS₂ nanoassemblies allows easy cell encapsulation without adversely affecting cell viability (>85%) after 48 h as observed in the confocal microscopy image (green = live cell, red = dead cell).

MoS₂ nanoassemblies can be used to develop light-actuating structures using 3D bioprinting. The proposed vacancy-driven gelation can be widely applied to form hydrogels from different types of 2D nanomaterials for biomedical applications.

Supporting Information

Supporting Information is available from the Wiley Online Library or from the author.

Acknowledgements

M.K.J. and A.K.G. conceptualized the study. M.K.J., J.K.C., and J.L.G. performed the experiments. J.G. and N.A. performed cyclic voltammetry

and Raman spectroscopy, respectively. M.K.J., J.K.C., J.L.G., and J.G. analyzed the results. M.K.J. and A.K.G. wrote the manuscript and all authors revised and approved the manuscript. The authors would like to acknowledge Junfeng Xie (University of Science and Technology, China) and Rajesh Kappara (Applied Materials Inc., USA) for their valuable discussion and advice on MoS₂ properties. The authors also acknowledge Charles W. Peak for helpful discussion and input on rheological analysis. A.K.G. acknowledges funding from the National Institute of Biomedical Imaging and Bioengineering (NIBIB, R03 EB023454), Texas Engineering Experiment Station (TEES), and Texas A&M University Seed Grant.

Conflict of Interest

The authors declare no conflict of interest.

Keywords

2D nanomaterials, biomedical applications, molybdenum disulfide (MoS₂), nanoengineered hydrogels, nanocomposites

Received: April 11, 2017

Revised: June 9, 2017

Published online: July 24, 2017

- [1] a) D. Voiry, A. Goswami, R. Kappera, E. SilvaCecilia de Carvalho Castro, D. Kaplan, T. Fujita, M. Chen, T. Asefa, M. Chhowalla, *Nat. Chem.* **2015**, 7, 45; b) S. S. Chou, N. Sai, P. Lu, E. N. Coker, S. Liu, K. Artyushkova, T. S. Luk, B. Kaehr, C. J. Brinker, *Nat. Commun.* **2015**, 6, 8311; c) V. Nicolosi, M. Chhowalla, M. G. Kanatzidis, M. S. Strano, J. N. Coleman, *Science* **2013**, 340, 1226419.
- [2] D. J. Late, Y.-K. Huang, B. Liu, J. Acharya, S. N. Shirodkar, J. Luo, A. Yan, D. Charles, U. V. Waghmare, V. P. Dravid, C. N. R. Rao, *ACS Nano* **2013**, 7, 4879.
- [3] E. P. Nguyen, B. J. Carey, J. Z. Ou, J. van Embden, E. D. Gaspera, A. F. Chrimes, M. J. S. Spencer, S. Zhuiykov, K. Kalantar-zadeh, T. Daeneke, *Adv. Mater.* **2015**, 27, 6225.
- [4] B. Radisavljevic, A. Radenovic, J. Brivio, V. Giacometti, A. Kis, *Nat. Nanotechnol.* **2011**, 6, 147.
- [5] D. Voiry, J. Yang, M. Chhowalla, *Adv. Mater.* **2016**, 28, 6197.
- [6] Z. Hu, L. Wang, K. Zhang, J. Wang, F. Cheng, Z. Tao, J. Chen, *Angew. Chem., Int. Ed.* **2014**, 126, 13008.
- [7] U. Maitra, U. Gupta, M. De, R. Datta, A. Govindaraj, C. N. R. Rao, *Angew. Chem., Int. Ed.* **2013**, 52, 13057.
- [8] D. U. Lee, J. Fu, M. G. Park, H. Liu, A. Ghorbani Kashkooli, Z. Chen, *Nano Lett.* **2016**, 16, 1794.
- [9] S. S. Chou, B. Kaehr, J. Kim, B. M. Foley, M. De, P. E. Hopkins, J. Huang, C. J. Brinker, V. P. Dravid, *Angew. Chem., Int. Ed.* **2013**, 125, 4254.
- [10] D. Chimene, D. L. Alge, A. K. Gaharwar, *Adv. Mater.* **2015**, 27, 7261.
- [11] M. Chhowalla, H. S. Shin, G. Eda, L.-J. Li, K. P. Loh, H. Zhang, *Nat. Chem.* **2013**, 5, 263.
- [12] G. Ye, Y. Gong, J. Lin, B. Li, Y. He, S. T. Pantelides, W. Zhou, R. Vajtai, P. M. Ajayan, *Nano Lett.* **2016**, 16, 1097.
- [13] B. D. Fairbanks, S. P. Singh, C. N. Bowman, K. S. Anseth, *Macromolecules* **2011**, 44, 2444.
- [14] a) S. S. Chou, M. De, J. Kim, S. Byun, C. Dykstra, J. Yu, J. Huang, V. P. Dravid, *J. Am. Chem. Soc.* **2013**, 135, 4584; b) J.-S. Kim, H.-W. Yoo, H. O. Choi, H.-T. Jung, *Nano Lett.* **2014**, 14, 5941; c) T. Liu, C. Wang, X. Gu, H. Gong, L. Cheng, X. Shi, L. Feng, B. Sun, Z. Liu, *Adv. Mater.* **2014**, 26, 3433; d) S. Presolski, M. Pumera, *Mater. Today* **2016**, 19, 140.
- [15] W. Feng, L. Chen, M. Qin, X. Zhou, Q. Zhang, Y. Miao, K. Qiu, Y. Zhang, C. He, *Sci. Rep.* **2015**, 5, 17422.
- [16] J. Xie, H. Zhang, S. Li, R. Wang, X. Sun, M. Zhou, J. Zhou, X. W. Lou, Y. Xie, *Adv. Mater.* **2013**, 25, 5807.
- [17] S. Tongay, S. S. Varnoosfaderani, B. R. Appleton, J. Wu, A. F. Hebard, *Appl. Phys. Lett.* **2012**, 101, 123105.
- [18] P. Cheng, K. Sun, Y. H. Hu, *Nano Lett.* **2016**, 16, 572.
- [19] a) A. K. Gaharwar, S. M. Mihaila, A. Swami, A. Patel, S. Sant, R. L. Reis, A. P. Marques, M. E. Gomes, A. Khademhosseini, *Adv. Mater.* **2013**, 25, 3329; b) O. Akhavan, E. Ghaderi, A. Akhavan, *Bio-materials* **2012**, 33, 8017.